IVYSPRING INTERNATIONAL PUBLISHER

Theranostics

2019; 9(4): 961-973. doi: 10.7150/thno.30765

Research Paper

Silk Fibroin-Coated Nanoagents for Acidic Lysosome Targeting by a Functional Preservation Strategy in Cancer Chemotherapy

Mixiao Tan[1], Weiwei Liu[1], Fengqiu Liu[1], Wei Zhang[1], Hui Gao[1], Juan Cheng[1], Yu Chen[2], Zhigang Wang[1], Yang Cao[1]✉ and Haitao Ran[1]✉

1. The Second Affiliated Hospital of Chongqing Medical University & Chongqing Key Laboratory of Ultrasound Molecular Imaging, Chongqing, 400010, China.
2. State Key Lab of High-Performance Ceramics and Superfine Microstructure, Shanghai Institute of Ceramics, Chinese Academy of Sciences, Shanghai, 200050, P. R. China.

✉ Corresponding authors: caoyangcqu@hospital.cqmu.edu.cn and ranhaitao@hospital.cqmu.edu.cn

Received: 2018.10.17; Accepted: 2019.01.07; Published: 2019.01.25

Abstract

Background: Premature drug leakage and inefficient cellular uptake are stand out as considerable hurdles for low drug delivery efficiency in tumor chemotherapy. Thus, we established a novel drug delivery and transportation strategy mediated by biocompatible silk fibroin (SF)-coated nanoparticles to overcome these therapeutic hurdles.

Methods: we first synthesised a TME-responsive biocompatible nanoplatform constructed of amorphous calcium carbonate (ACC) cores and SF shells for enhanced chemotherapy by concurrently inhibiting premature drug release, achieving lysosome-targeted explosion and locally sprayed DOX, and monitoring via PAI, which was verified both *in vitro* and *in vivo*.

Results: The natural SF polymer first served as a "gatekeeper" to inhibit a drug from prematurely leaking into the circulation was demonstrated both *in vitro* and *in vivo*. Upon encountering TMEs and targeting to the acidic pH environments of lysosomes, the sensitive ACC nanoparticles were gradually degraded, eventually generating a large amount of Ca^{2+} and CO_2, resulting in lysosomal collapse, thus preventing both the efflux of DOX from cancer cells and the protonation of DOX within the lysosome, releasing multiple hydrolytic enzyme to cytoplasm, exhibiting the optimal therapeutic dose and remarkable synergetic therapeutic performance. In particular, CO_2 gas generated by the pH response of ACC nanocarriers demonstrated their imaging capability for PAI, providing the potential for quantifying and guiding drug release in targets.

Conclusion: In this work, we constructed TME-responsive biocompatible NPs by coating DOX-preloaded ACC-DOX clusters with SF via a bioinspired mineralization method for efficient therapeutics. This functional lysosome-targeted preservation-strategy-based therapeutic system could provid novel insights into cancer chemotherapy.

Key words: silk fibroin coating, amorphous calcium carbonate, acid-responsive, premature drug release, cancer chemotherapy

Introduction

Despite remarkable progress in cancer chemotherapy through the utilization of nanocarriers as drug delivery vehicles, imperative major obstacles emerge when using chemotherapeutic drugs in cancer treatment, since most of these drugs have dose-limiting toxicity and inefficient intracellular accumulation. Premature drug leakage and inefficient cellular uptake also stand out as considerable hurdles

in cancer chemotherapy. It has been reported that only 0.7% of injected nanodrugs actually accumulate in tumor tissue [1]. In addition, unexpected drug release can cause severe side effects in other organs. Doxil®, the first FDA-approved liposomal drug, has been utilized in clinic for over 20 years. However, several clinical trials have disclosed that Doxil® does not show expected antitumor efficacy advantages over free DOX in long-term treatment [2-4], which is largely attributed to the fact that when Doxil® is endocytosed by tumor cells, it is trapped in endo-lysosomes and is unable to release DOX into the cell nucleus to exert its antitumor effect [5]. In addition, the MDR of cancer cells mediated by some membrane transporters can actively promote the efflux of DOX from cancer cells. Lysosomes are membrane-bound cytoplasmic organelles that are considered digestion and recycling compartments during the process of endocytosis, phagocytosis, drug resistance and signal transduction [6, 7]. The destruction of lysosome membranes releases multiple hydrolytic enzyme into the cytoplasm, further leading to autolysis, which is promising for cancer therapy [8]. Lysosomal dysfunction may lead to numerous diseases, such as Alzheimer's disease, storage diseases and cancer [9, 10]. Therefore, lysosomal targeting and destruction is a promising drug delivery and transportation strategy in cancer chemotherapy. Since lysosomes are more acidic (pH ca. 5.5) than any other subcellular organelles [11], the ideal lysosome-targeting agent should be pH-sensitive, biocompatible and hydrophilic. Amino, morpholine, and methylcarbitol functional groups are always designed into lysosome-targeted compounds [12-14]. Though designed nanocarriers are increasingly reported, their potentially low biocompatibility and poor therapeutic effect have limited their application in chemotherapy [15-18]. In view of these inadequacies, a smart nanoplatform-based drug delivery system must urgently be explored.

SF is a natural polymeric biomaterial obtained from mulberry silkworms of the species Bombyx mori. SF shows low toxicity and good biocompatibility and has an intrinsic capability to respond to pH changes [19-21]. Therefore, it can be used in lysosomotropic delivery systems without chemical modification [22]. In an environment with low pH, SF loses its overall acidic surface properties and negative net charge [23]. Thus, payloads, which are absorbed by SF by electrostatic interactions and chelation, are released from the nanocarriers. Thus, controlled drug release could be achieved by changing the electrostatic interaction between the silk and the loading agents. To achieve endosomal targeting and escape, lysosomes should be destroyed. Due to its good biocompatibility, ACC has been used in various biomedical applications, especially in drug delivery. ACC can generate a large amount of CO_2 gas in response to acidic pH environments, which makes ACC nanoparticles a good candidate for lysosome targeting and destruction.

In this regard, in the rational design, we constructed a tumor acidity-responsive biocompatible nanoplatform for enhanced chemotherapy by concurrently inhibiting premature drug release, achieving lysosome-targeted explosion and locally sprayed DOX, and monitoring via PAI. In particular, SF, as an FDA-approved natural protein, possesses excellent swelling and pH-responsive properties [24], acting as a gatekeeper when coated on the surface of ACC nanoparticles, modifying and stabilizing the phase of ACC. As shown in **Figure 1**, Upon encountering a weakly acidic environment, the size of ACC-DOX-SF NPs gradually decreases, which is beneficial for the efficient accumulation of NPs in the tumor region. After targeting the lysosomes, the lower pH accelerates the decomposition of the NPs into Ca^{2+}, CO_2 and DOX, leading to the destruction of the lysosome, followed by the release of proteolytic enzyme, preventing both the efflux of DOX from cancer cells and the protonation of DOX within the lysosome, thus amplifying cancer therapy. Meanwhile, the generated CO_2 and released DOX could be monitored by PAI, realizing "all-in-one" visualized cancer chemotherapy.

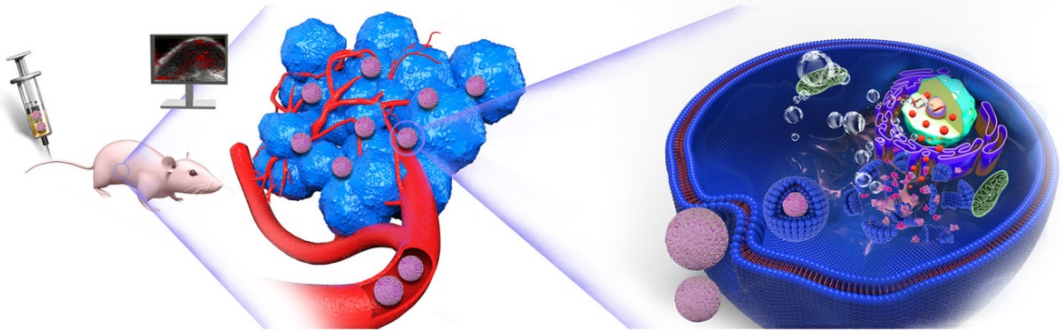

Figure 1. Schematic illustration of drug transportation strategy for chemotherapy by concurrently inhibiting premature drug leakage, achieving lysosome-targeted explosion and locally sprayed DOX, monitored via PAI.

Materials and Methods

Materials

NH_4HCO_3, $CaCl_2 \cdot 2H_2O$ and Na_2CO_3 were purchased from Sigma Aldrich (St. Louis, MO, USA). DOX was purchased from Adamas-beta (Shanghai, China). Silkworm cocoons were obtained from the Sericultural Research Institute, Chinese Academy of Agricultural Sciences. Penicillin–streptomycin solution, DAPI and Lysotraker Green were perchased from Beyotime Biotechnology. CCK-8 was bought from Dojindo (Japan). FITC-CD31 antibody, TUNEL, PCNA, FITC-CD3 antibody, CD4-PE antibody and CD8-APC antibody were obtained from Servicebio Technology Co., Ltd (Wuhan, China). Mouse IgG ELISA kit, Mouse IgM ELISA kit and Mouse IgA ELISA kit were purchased from Lianke Technology Co., Ltd (Hangzhou, China). All other chemicals and reagents were of analytical grade and purchased from Sinopharm Chemical reagent Co., LTD (Shanghai, China).

Preparation of the silk fibroin (SF)

An appropriate amount of silkworm cocoons was boiled in Na_2CO_3 (0.02 M) solution twice, 1 h each time, and then rinsed with double-distilled water several times to fully wash out the sericin. Then, the obtained SF was immersed in a LiBr (9.2 M) solution at 60°C for 5 h. Afterward, the SF was dialyzed (MW = 3.5-5 kDa) against deionized water for 3 days, collected, filtered, and freeze dried.

Synthesis of ACC-DOX-SF NPs

ACC-DOX-SF NPs were synthesized via a gas diffusion method. $CaCl_2 \cdot 2H_2O$ (200 mg) and DOX (5 mg, predissolved in DMSO) were dissolved in anhydrous ethanol (10 mL) and stirred for 0.5 h. Then, a proper amount of SF (predissolved in deionized water) was added, and the obtained solution was transferred to a glass bottle with 200 mL anhydrous ethanol and covered with parafilm with several small holes. Then, the bottle was placed in a vacuum drying chamber, surrounded by four dishes containing ammonia bicarbonate (~3-4 g). After 25 h of reaction, the particles were centrifuged at 8000 rpm and dried in air before use.

ACC-DOX-SF NPs Characterization

The morphology of ACC-DOX-SF NPs was observed using a TEM (JEM-1200, JEOL, Japan) and FESEM (Hitachi SU8010, Japan). DLS measurements were performed using a Zetasizer Nano ZS90 (Malvern, USA). The UV-Vis-NIR spectrum of NPs were detected using a UV-Vis-NIR spectrophotometer (UV-3600, Shimadzu, Japan). The polymorphs of different NPs were measured by XRD (Rotaflex RU-200, Rigaku, Japan) and FTIR (Bruker Tensor 27 spectrometer). TG analyses of the NP powders were conducted by a STA-449C (Netzsch Co.) machine.

pH-triggered drug release *in vitro*

For DOX loading, 0.01 g of ACC-DOX-SF NPs was dissolved in diluted HCl (pH = 4, 100 mL) and stirred overnight. Then, the concentration of DOX was determined by UV–Vis-NIR spectroscopy at 490 nm. For SF loading, the concentration was measured using a BCA protein assay kit according to the manufacturer's protocol.

ACC-DOX-SF NPs were dissolved in acetate buffer with different pH values (pH = 5.5, 6.5, 7.4) at 37°C with a stirring speed of 120 rpm. At every predetermined time point (5 min, 10 min, 15 min, 30 min, 1 h, 2 h, 4 h, 8 h, 12 h, 24 h and 36 h), a 2 mL aliquot was withdrawn and centrifuged to collect the supernatant. The DOX released in the obtained supernatant was analyzed by UV-Vis-NIR spectra.

Quantitation of generated CO_2

Different concentrations of ACC-DOX-SF NPs (2 mg/mL, 4 mg/mL, 6 mg/mL and 8 mg/mL) were dissolved in acetate buffer with various pH values, from 5.5 to 7.4, in vials sealed with rubber stoppers and connected to the air quality meter. Then, the vials were magnetically stirred over 24 h. The amounts of CO_2 generated from ACC-DOX-SF NPs were quantitatively measured using an air quality meter (IAQ- 7515, TSI Inc., Shoreview, MN, USA).

Intracellular uptake and lysosome-targeted destruction of ACC-DOX-SF NPs

The 4T1 cell line was purchased from ATCC (Rockville, MD, USA) and cultured with Roswell Park Memorial Institute (RPMI) 1640 medium (Gibco BRL, USA) supplemented with 10% FBS (HyClone, USA) and 1% penicillin–streptomycin solution (Beyotime Biotechnology, China) under standard conditions (37°C, 5% CO_2). Cell experiments were conducted on the growth rate of subcultured cells in the logarithmic phase.

To characterize the intracellular uptake capability of ACC-DOX-SF NPs, 5×10^4 4T1 cells were spread onto laser confocal microscopy dishes and incubated under standard conditions (37°C, 5% CO_2). After 24 h, the culture medium was replaced with serum-free culture medium containing ACC-DOX-SF NPs (concentration of DOX was 5 μg/mL). At predetermined time intervals (2 h, 6 h and 12 h), the treated cells were washed with sterile PBS and fixed with 4% paraformaldehyde for 10 min. The fixed cells were washed with PBS, and the nuclei of the 4T1 cells were stained blue by DAPI. Fluorescence images were obtained by a CLSM (Nikon A1, Japan).

To evaluate the lysosome-targeting capacity, the lysosomes were labeled with Lysotracker Green probe to identify the localization of intracellular ACC-DOX-SF NPs. After 4 h of incubation with free DOX, ACC-DOX-SF NPs, or treated ACC-DOX-SF NPs (i.e., NPs preincubated in serum-free culture medium with a pH value of 6.5 for 2 h), cells were incubated with Lysotracker Green for 30 min to label the lysosomes. The treated cells were washed with PBS, stained with Hoechast33258 for 10 min, and then washed with PBS several times to remove the residual dye. The lysosomal localization of ACC-DOX-SF NPs was confirmed by CLSM. The PC coefficients and intensity line profiles of ROI were also analyzed. Furthermore, time-dependent (2 h, 4 h, 6 h, 12 h) incubation with ACC-DOX-SF NPs at pH 6.5 was observed by TEM. At predetermined time intervals, cells were digested, centrifuged and fixed with aldehyde fixatives, then sent to electron microscopy room.

To verify the chemotherapy efficacy of NPs *in vitro*, 4T1 cells were separately seeded onto 96-well plates at a density of 1×10^4 and onto 6-well plates at a density of 3×10^5 for 24 h of incubation. Different concentrations of ACC-DOX-SF NPs, free DOX, ACC-SF NPs and treated ACC-DOX-SF NPs (i.e., preincubated in serum-free culture medium with pH value of 6.5 for 2 h) were added to each well for another 12 h of incubation. Afterward, cells were washed with PBS 2-3 times. Cell viabilities were measured by a CCK-8 assay according to the manufacturer's protocol or analyzed by CytoFLEX FCM (Beckman Coulter Ltd., USA).

Animal model

All animal experiments were conducted following the Guide of Care and approved by the Chongqing Medical University Laboratory Animal Center. To establish 4T1 tumor models, female nude mice were subjected to standard subcutaneous inoculation.

Gatekeeper efficiency of SF

Equal amounts of ACC-DOX NPs and ACC-DOX-SF NPs were weighted and separately suspended in PBS (pH 7.4) containing 10% FBS at 37°C with a stirring speed of 120 rpm. At different time points (1 d, 2 d, 3 d, 4 d, 5 d, 6 d, 7 d), 2 mL samples were withdrawn and centrifuged to collect the supernatant and then measured by UV-Vis-NIR spectra.

To mimic the pH-triggered release behavior of NPs in blood circulation, NPs were immersed in PBS containing 10% FBS with pH value of 7.4 for 7 h. Then, the suspension solution was centrifuged, the supernatant was discarded, and the sediment was resuspended in a similar solution with a pH value of 6.5 for 0.5 h. Afterward, the obtained sediment was treated following the same procedure previously described and resuspended in a similar solution with a pH value of 5.5 for 0.5 h. At different time points, 2 mL samples were withdrawn, photographed and centrifuged to collect the supernatant, and then, their UV-Vis-NIR spectra were recorded. Meanwhile, the size changes of NPs were measured by DLS.

To evaluate the gatekeeper efficiency of SF *in vivo*, tumor-bearing mice were divided into 3 groups (n = 15), and each group of mice was intravenously administered with ACC-DOX-SF NPs, ACC-DOX NPs or free DOX at an equivalent dose of 5 mg DOX/kg. Then, each of group was divided into 5 subgroups (n = 3), labeled using ear studs. At each predetermined time point (2 h, 4 h, 8 h, 12 h, and 24 h post injection), some labeled mice were sacrificed, and then, plasma, main organs (heart, liver, spleen, lung, kidney) and tumor tissue were harvested, weighed, immersed in extraction agent (trichloromethane: methyl alcohol = 4:1) and centrifuged. Finally, the obtained supernatants were analyzed using fluorescence measurements.

Besides, the metabolism of ACC-DOX-SF NPs, ACC-DOX NPs and DOX was investigated in Balb/c mice (n=3, housed in metabolic cages), ACC-DOX-SF NPs, ACC-DOX NPs or free DOX in saline were intravenous injected into mice at an equivalent dose of 5 mg DOX/kg per mouse. Then exercted urine and faeces were collected at different time intervals (6 h, 24 h, 36 h, 48 h, 72 h, 96 h, 120 h, 144 h and 168 h). Finally, the DOX content in urine and faeces were analyzed by fluorescence measurements.

PA-guided drug release behavior *in vivo*

ACC-DOX-SF NPs were irradiated by the Vevo Laser system (Visual Sonics, Inc., Toronto, ON, Canada) to determine the optimal excitation wavelength (the scanning range of excitation wavelengths was from 680 nm to 970 nm). Then, the PA signals of CO_2 and dd H_2O were determined. For *in vitro* PAI, ACC-DOX-SF NPs (2 mg/mL) was immersed in acetate buffer solution at various pH values (pH 5.5, pH 6.6 and pH 7.4) in a 3% agarose gel phantom. Then, PA images were recorded, and the PA signal of the ROI was measured at different time points. For *in vivo* PAI, 200 μL of ACC-DOX-SF NPs in sterile saline, ACC-DOX NPs in sterile saline or free DOX in sterile saline (DOX = 5 mg/kg per mouse) was intravenously injected into each nude tumor-bearing mouse. Saline was used for the control group. Then, at 0 h, 0.5 h, 1 h, 2 h, and 4 h post injection, PA images of each mouse were recorded, and values were measured in the ROI.

In vivo chemotherapeutic efficacy of ACC-DOX-SF NPs

To evaluate the *in vivo* chemotherapy efficiency of ACC-DOX-SF NPs, twenty 4T1 tumor-bearing mice (~60-80 mm^3 in tumor size) were randomly divided into four groups (n = 5 per group), including ACC-DOX-SF NPs, ACC-DOX NPs, free DOX and saline. Each group of mice was intravenously injected 4 times with 200 μL of the different agents in sterile saline at an equivalent dose of 5 mg DOX/kg per mouse every 5 days. The tumor volume was calculated by volume = length × $width^2$ / 2 [25-27]. Tumor volume changes were normalized by the relative tumor volumes V/V_0 (V_0 means the initial tumor volume). After 20 days of treatment, all mice were sacrificed, and the major organs (tumor tissue, heart, liver, spleen, lung, kidney and brain) were collected for H&E, TUNEL or PCNA staining. All tissues were photographed using an optical microscope (Olympus DP70, Canada) at 200× magnification.

Furthermore, the extracted tumors were subjected to cryotomy, the obtained frozen sections were treated with EDTA (PH 8.0), PBS (PH 7.4), BSA and anti-CD31 antibodies following the manufacturer's instructions, then dropwise added into FITC labeled goat anti-mouse IgG and stained with DAPI. After washed with PBS several times, the sections were visualized by CLSM.

Biosafety Assay of ACC-DOX-SF NPs

24 Balb/c mice (5-6 weeks) were divided into eight groups: (1) control group, (2) 1 h group, (3) 3 h group, (4) 6 h group, (5) 12 h group, (6) 24 h group, (7) 48 h group and (8) 72 h group. The blood samples were collected after 1 h, 3 h, 6 h, 12 h, 24 h, 48 h and 72 h intravenous administration of the saline or ACC-DOX-SF NPs (an equivalent dose of 5 mg DOX/kg per mouse). Then blood routine examination and serum biochemistry indexes including blood urea nitrogen (BUN), alanine aminotransferase (ALT), aspartate aminotransferase (AST), alkaline phosphatase (ALP) were conducted. To evaluate the immunotoxicity of NPs, mice were treated with ACC-DOX-SF NPs, ACC-SF NPs, DOX or saline, separately. At 1 d, 3 d, 7 d and 14 d intravenously injection, the mice were sacrificed, then the blood samples were collected and stained with anti-CD3-FITC, anti-CD4-PE and anti-CD8-APC according to the manufacture's protocols, then analyzed on a FACS Vantage. Furthermore, immunoglobulin A (IgA), immunoglobulin M (IgM), immunoglobulin G (IgG) were analyzed with use of ELISA kits according to the manufacturer's protocols.

Statistical analyses

All experiments were conducted in triplicate. One-way ANOVA and two-tailed Student's t-tests were performed in SPSS 23.0 statistical software (SPSS Inc., Chicago, USA). The results from each group are presented as the mean ± SD. *: $p < 0.05$, **: $p < 0.01$, ***: $p < 0.001$.

Results and Discussion

Synthesis of ACC-DOX-SF NPs

The fabrication process of ACC-DOX-SF NPs is illustrated in **Figure 2A**, in which the NPs were simply synthetized via a bioinspired mineralization method in an enclosed chamber, utilizing ethanol as the reaction control medium and ammonium bicarbonate as the source of carbon dioxide [28]. During this procedure, Ca^{2+} chelated with DOX to form Ca-DOX clusters; then, SF was coated onto the surface of ACC-DOX NPs via the interaction between $-NH_2$ groups and CO_3^{2-} groups on the clusters [29]. As illustrated in **Figure 2B**, the hydrodynamic size of the resulting ACC-DOX-SF NPs was determined to be 179 ± 3 nm by DLS, with a solid spherical morphology and a thin corona (inset picture in **Figure 2B**). The ultraviolet (UV) absorption band of the NPs in deionized water showed distinct characteristic peaks at 545 nm and 585 nm, whereas when the NPs were dispersed in diluted HCl, the peaks at 545 nm and 585 nm blueshifted to 475 nm and 495 nm [30-32], respectively, and the color of the resuspension solution changed from purple to orange, which could indicate that DOX tightly chelated with Ca^{2+} and was undamaged after release [33]. Moreover, the UV characteristic peak of SF at 275 nm was found in the absorption spectrum of ACC-DOX-SF NPs, which verified the successful encapsulation of SF in the NPs (**Figure 2C**). Thermogravimetric (TG) analysis is displayed in **Figure 2D**. For ACC-DOX NPs, the weight loss of 61.4% from approximately 380°C to 680°C could probably be attributed to the decomposition of DOX and $CaCO_3$ into calcium oxide and CO_2 [34]. For ACC-DOX-SF NPs, the process of thermal decomposition was slower than that of ACC-DOX NPs from 0°C to 580°C, and the weight loss was 48.6% eventually in ACC-DOX-SF NPs, lower than that of ACC-DOX NPs (61.4%), implying that the chemical stability of SF was significantly enhanced in the ACC-DOX-SF nanostructure.

To confirm that adding SF could regulate and control the formation of ACC, we established subgroups of NPs with different concentrations of SF and analyzed them using Fourier-transform infrared (FTIR) spectroscopy. **Figure S1, S2** exhibited the shape and size of magnified TEM images of

ACC-DOX-SF NPs with different amount of SF. The thickness of obtained SF corona became thicker with increased concentration of SF and the coated SF corona got heterogeneous when the concentration of SF increased to 3.5 mg/mL. The size of NPs was changed from 180 ± 5 nm (SF: 1.5 mg/mL) to 182 ± 3 nm (SF: 2.5 mg/mL), yet to 188 ± 3 nm (SF: 3.5 mg/mL), accordingly. **Figure 2E** presented the FTIR spectra of SF, $CaCO_3$, $CaCO_3$-SF_1 (SF: 1.5 mg/mL), $CaCO_3$-SF_2 (SF: 2.5 mg/mL) and $CaCO_3$-SF_3 (SF: 3.5 mg/mL). The split peaks at 1418 cm^{-1} and 1475 cm^{-1} and the strong v_2 absorption band at 866 cm^{-1} were characteristic of the amorphous phase of $CaCO_3$ [35-36]. The appearance of the v_4 symmetric vibration at 713 cm^{-1} and the sharp v_3 band (1475 cm^{-1}) proved the formation of the calcite phase [37]. The weak v_4 absorption band at 745 cm^{-1} represented the aragonite phase. Clearly, the obtained $CaCO_3$ NPs without SF were in the calcite phase. When concentration of added SF was 1.5 mg/mL, the obtained $CaCO_3$ NPs contained three phases: calcite, amorphous and aragonite phases. When the SF concentration was increased to 3.5 mg/mL, the resultant NPs mainly contained the amorphous phase. Similar results were proven by the X-ray diffraction (XRD) assay in **Figure 2F**. $CaCO_3$ NPs presented the formation of pure calcite, which matched well with the International Centre for Diffraction Data (ICDD) database PDF #83-0578. Meanwhile, $CaCO_3$-SF_1 and $CaCO_3$-SF_2 presented a mixture of vaterite and calcite based on the ICDD database PDF #72-0506. Noticeably, the obtained $CaCO_3$-SF_3 mainly resulted in the formation of ACC, which showed no distinct diffraction peaks [38].

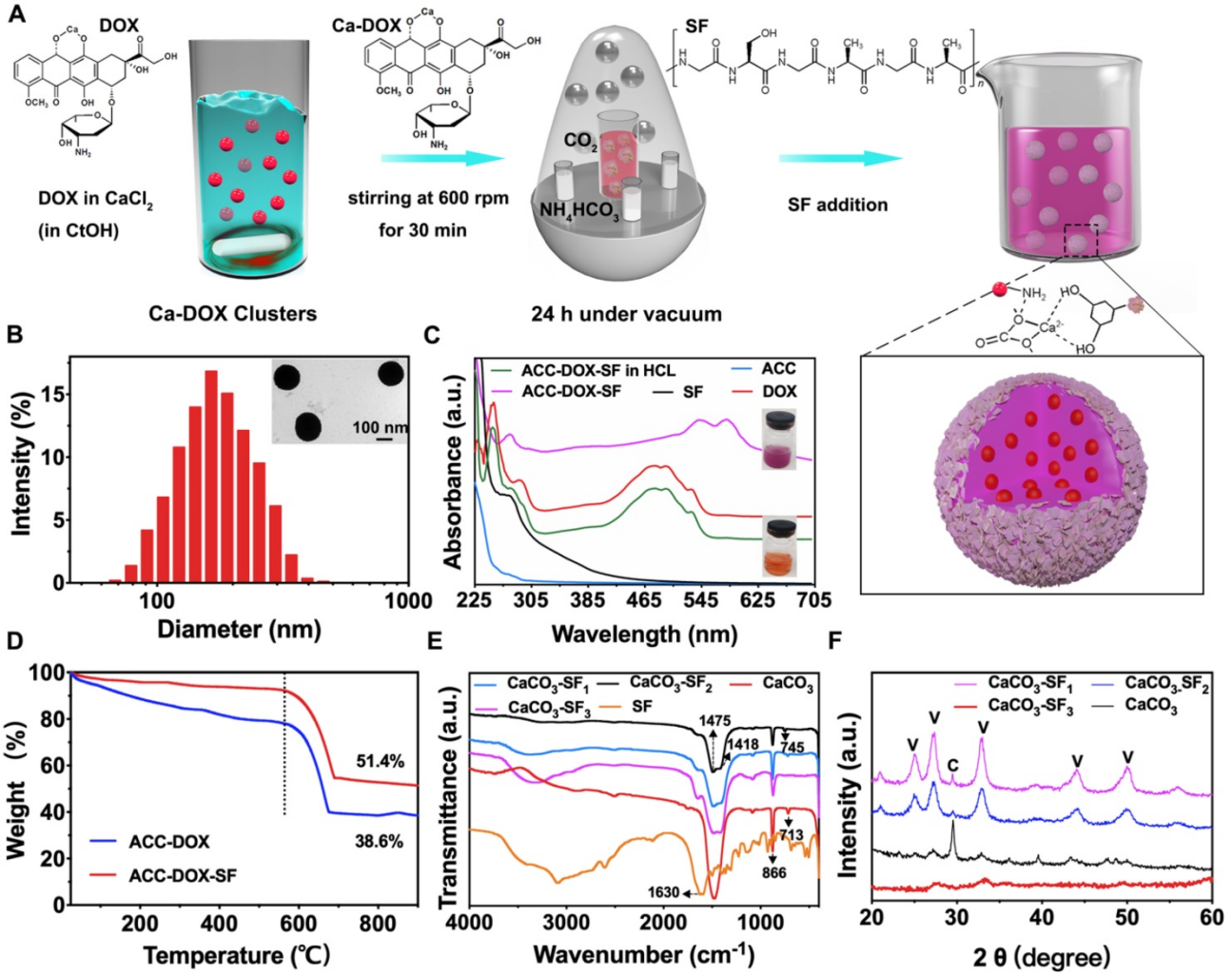

Figure 2. Characterization of ACC-DOX-SF NPs. (A) The fabrication process of ACC-DOX-SF NPs. (B) Hydrodynamic size distribution and representative TEM image (inset) of ACC-DOX-SF NPs. (C) UV-Vis spectra of a solution of ACC-DOX-SF NPs in dilute HCl (ACC-DOX-SF NPs in HCl); pure ACC; and solutions of ACC-DOX-SF NPs, pure DOX and pure SF in deionized water. The upper inset image is a purple suspension of ACC-DOX-SF NPs in deionized water. The lower inset image is an orange suspension of ACC-DOX-SF NPs in dilute HCl. (D) TG curves of the ACC-DOX-SF NPs and ACC-DOX NPs. (E, F) FTIR spectra and XRD patterns of SF, $CaCO_3$ NPs (without the addition of SF), $CaCO_3$-SF_1 NPs (the concentration of SF was 1.5 mg/mL), $CaCO_3$-SF_2 NPs (the concentration of SF was 2.5 mg/mL) and $CaCO_3$-SF_3 NPs (the concentration of SF was 3.5 mg/mL).

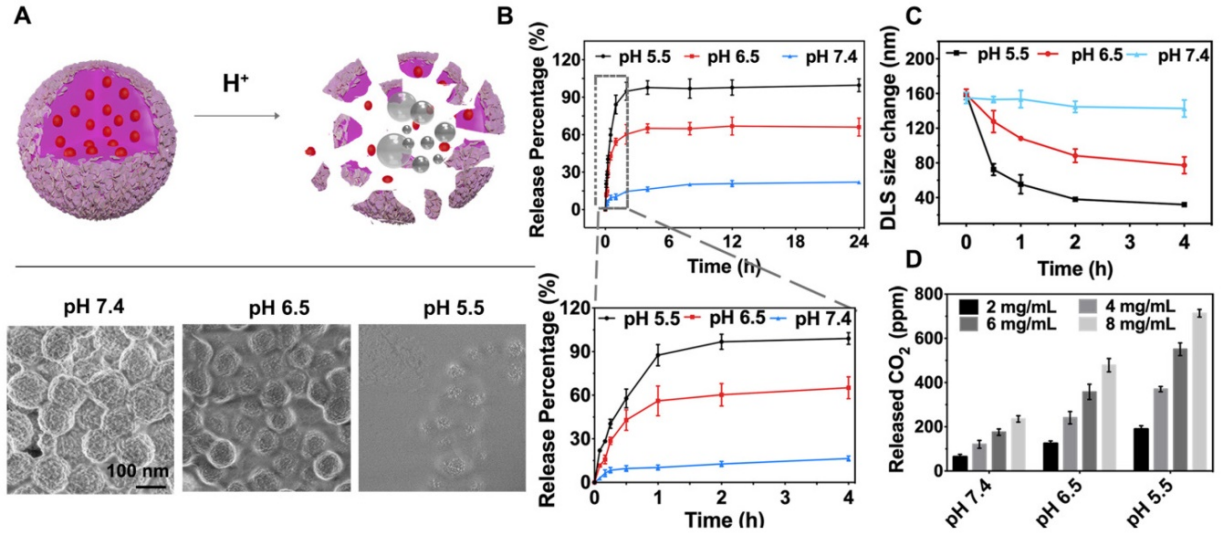

Figure 3. *In vitro* pH-responsive DOX release. (A) Schematic illustration of the acid-responsive decomposition of ACC-DOX-SF NPs and their corresponding FESEM images after incubation in PBS at different pH values (5.5, 6.5 and 7.4) for 2 h. (B) pH-responsive drug release curves of DOX from ACC-DOX-SF NPs. The lower picture is a magnification of the DOX release profile within 4 h. (C) Time-dependent changes in the size of NPs suspended in different pH values. (D) Quantitative CO_2-generation profiles of the ACC-DOX-SF NPs at different concentrations and incubated in acetate buffer solution with different pH values. The results are expressed as the mean ± standard deviation (SD), *P < 0.05, **P < 0.01, or ***P < 0.001.

pH response of ACC-DOX-SF NPs

An effective drug carrier allows controlled drug release dynamics inside tumor tissue. To visualize the drug release behavior of the obtained ACC-DOX-SF NPs, their decomposition profiles were thus explored by incubation at pH 5.5, pH 6.5 and pH 7.4, which mimicked the microenvironments of lysosomes, tumors and blood, respectively [39]. As shown by field-emission scanning electron microscopy (FESEM), the NPs were stable at pH 7.4 but gradually dissociated under mildly acidic conditions (pH 6.5 and pH 5.5) (**Figure 3A**). As a result of this encouraging pH-responsive decomposition behavior, the capability of the NPs as an efficient lysosome-targeted drug carrier was then investigated. The loading content of DOX in ACC-DOX-SF NPs was measured to be 7.4 wt % by UV-Vis spectroscopy, while SF content was determined to be 29.7 wt % by the BCA method. The release profiles of DOX from NPs were quantitatively studied by immersing the NPs in PBS with various pH values for varying time intervals. Approximately 93.2% of the loaded DOX was released from ACC-DOX-SF NPs incubated at pH 5.5 for 24 h, which was much higher than the 62.7% and 17.7% release from NPs incubated in PBS at pH 6.5 and 7.4, respectively (**Figure 3B**). Interestingly, the significant burst of released DOX was constrained to 2 h under neutral conditions (pH 7.4), which may be explained by the exceptional swelling properties of SF, leading to numerous water channels in the porous network of NPs when incubated in water, which severely inhibited premature drug release. Accordingly, the time-dependent change in the size of NPs at different time intervals was observed by DLS (**Figure 3C**). As time went on, the NPs became increasingly smaller at pH 6.5, which was beneficial to the cellular internalization [40-42]. Whereas this shrinking process was intensely accelerated at pH 5.5 but was less obvious at pH 7.4. In addition, CO_2 generation from ACC-DOX-SF NPs was quantified using an air quality meters. The concentration- and acidity-dependent results are presented in **Figure 3D**. Furthermore, the zeta potential of the NPs was -10.2 mV at pH 5.5, -13.4 mV at pH 6.5 and -22.3 mV at pH 7.4 (**Figure S3**), of which charges created a repulsive electric potential between NPs and inhibited coalescence and enhanced stability [43-44].

Gatekeeper efficiency of SF *in vitro* and *in vivo*

Minimizing premature drug release benefits high-efficiency chemotherapy and drastically decreases systemic the side effects of chemotherapeutics. Therefore, encouraged by the prominent drug release profiles of NPs under physiological conditions (pH 7.4), the gatekeeping capability of SF to prevent premature drug release was studied next. To mimic blood physiological conditions, ACC-DOX-SF NPs were suspended in PBS at pH 7.4 containing 10% FBS at 37°C and measured at different time interval. As shown in **Figure 4A**, the drug leakage from the ACC-DOX-SF NPs was 15.6%, apparently lower than that of ACC-DOX NPs (36.4%), showing that SF provided an outstanding gatekeeper effect *in vitro*. To gain further insight into the pH-triggered release behavior of the NPs in blood circulation, NPs were successively immersed in PBS containing 10% FBS with pH values of 7.4, 6.5 and 5.5. As shown in **Figure 4B**, when the NPs were transferred from a solution

with pH 7.4 to one with pH 6.5, the decomposition process was accelerated, and it was even faster when the NPs were immersed in a solution with a pH value of 5.5. Meanwhile, the size of the NPs decreased following the same trend as that of drug release, and the color of the resuspension solution turned from purple to red to orange, further elucidating the excellent gatekeeper efficiency of SF and the high sensitivity of the NPs.

To further verify the gatekeeper efficiency of SF *in vivo*, we first examined the delivery of DOX in TME-responsive NPs among tumor-bearing Balb/c mice. At a predetermined time, the mice were sacrificed, and then, their blood, tumors and major organs were measured and compared. As shown in **Figure 4C**, the ACC-DOX-SF NPs could circulate in blood for a longer time than free DOX and ACC-DOX NPs, with an 8-fold and 12-fold increase in half-life, respectively. In addition, within the tumor, the amounts of drugs delivered in the ACC-DOX-SF NPs group was higher than those in the free DOX group (3-fold increase) and ACC-DOX NPs group (2-fold increase). Moreover, the amounts of DOX in the heart, liver, spleen, lung and kidney in the various groups at different time intervals are exhibited in **Figure 4D**. As time continued to 24 h, the ACC-DOX-SF NPs in the major organs retained a higher concentration than ACC-DOX NPs and free DOX, which was in accordance with the blood circulation results. Accordingly, SF could be inferred to play a pivotal role in inhibiting premature drug release during the delivery process and exhibits excellent gatekeeper efficiency. As shown in **Table S1-6** and **Figure 4E-F**, the majority of ACC-DOX-SF NPs, ACC-DOX NPs and free DOX were renally excreted and the minority excreted through faeces, deduced that the renal clearance were the main excretion route, which was consistent with results of previous studies on DOX pharmacokinetics [45-48]. Besides, the metabolism of ACC-DOX-SF NPs and ACC-DOX NPs showed a relatively low cumulative excretion rate both in urine and faeces, the discharge rate of DOX increased with

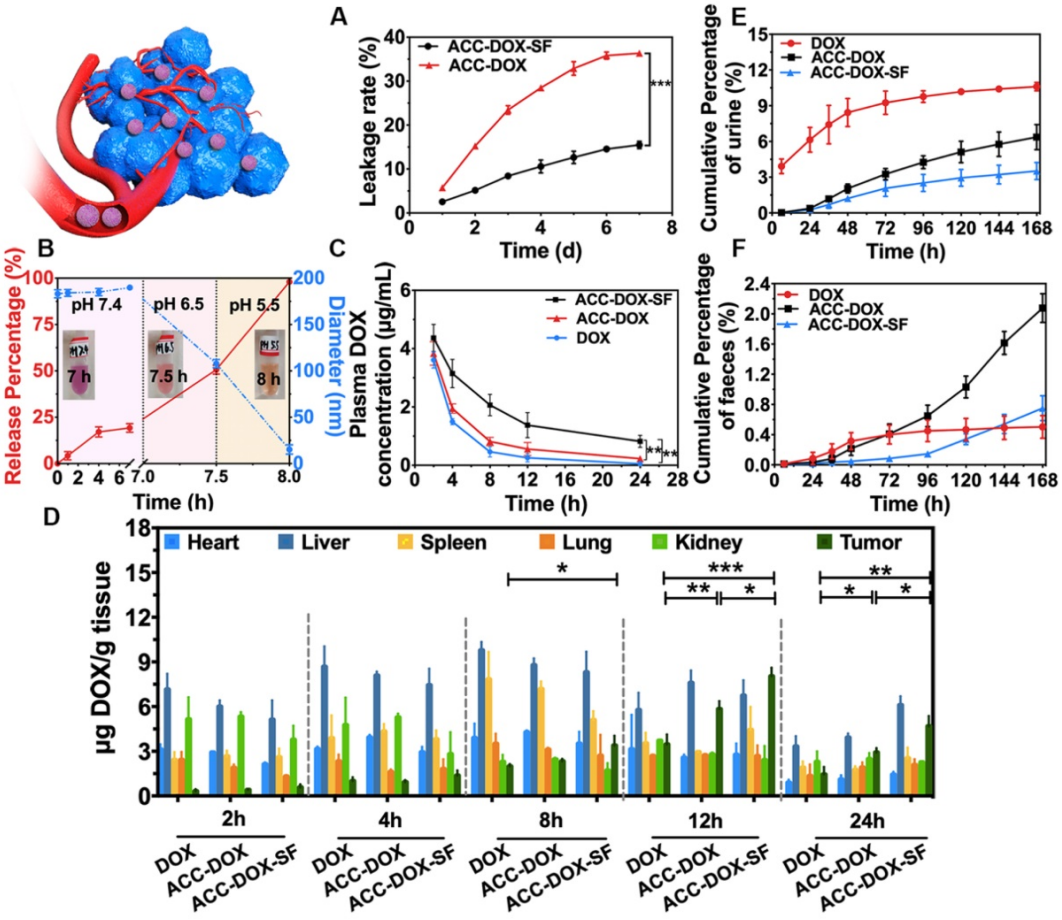

Figure 4. Gatekeeper efficiency of SF *in vivo* and *in vitro*. (A) Leakage rate of DOX released from ACC-DOX-SF NPs suspended in PBS (pH 7.4) containing 10% FBS at 37°C. The data points represent the mean ± S.D. (n = 3). (B) Drug release and size changes of NPs successively immersed in PBS containing 10% FBS with a pH value of 7.4 for 7 h, pH 6.5 for 0.5 h and pH 5.5 for 0.5 h. (C) The time-dependent plasma concentration of DOX after intravenous injection with ACC-DOX-SF NPs, ACC-DOX NPs and DOX. (D) Distribution of DOX in major organs and tumors after intravenous injection with ACC-DOX-SF NPs, ACC-DOX NPs and free DOX. (E) Total cumulative amount of DOX excreted in mice urine after a single intravenous injection of DOX, ACC-DOX NPs or ACC-DOX-SF NPs, separately (n=3). (F) Total cumulative amount of DOX excreted in mice faeces after a single intravenous injection of DOX, ACC-DOX NPs or ACC-DOX-SF NPs, separately (n=3). The results were expressed as the mean ± SD (n = 3, *P < 0.05, **P < 0.01, ***P < 0.001).

increasing time and reached the dynamic balance during the study period, which could be achieved prolonged circulation time.

Intracellular uptake and lysosome-targeted destruction of ACC-DOX-SF NPs

Efficient, effective intracellular uptake of ACC-DOX-SF NPs is central to improving its chemotherapy efficacy to maximize killed cancer cells. Therefore, to investigate the intracellular uptake capacity of NPs, confocal images of cells cocultured with NPs for different times were recorded (**Figure 5A**). After 2 h of coculturing, an obvious red fluorescence of ACC-DOX-SF NPs was observed in the cytoplasm. With increasing incubation time, many more NPs accumulated in the cytoplasm and even in the cell nucleus, which demonstrated the remarkable capacity of NPs to be taken up by tumor cells. Cell viability was assayed using CCK-8, and the ACC-SF nanocarrier showed no obvious cytotoxicity to normal cells (HUVECs), even at a higher concentration of 0.5 mg/mL (**Figure 5B**). When loaded with DOX, the cell viability of the cancer cells (4T1 cells) decreased sharply, and the downswing depended on concentration (**Figure 5C**). Similar results were verified by FCM measurements. Among the various treatments, the group treated with ACC-DOX-SF NPs showed the highest cell apoptotic ratio (**Figure S4**). Then, the lysosome-targeting destruction capability of ACC-DOX-SF NPs was evaluated by costaining experiments. To imitate the acidic microenvironment in tumors, ACC-DOX-SF NPs were presuspended in cell culture medium at 37°C, and the pH was adjusted to 6.5 using a sterile diluted HCl solution before incubation with the 4T1 cells. As shown in **Figure 5D**, free DOX quickly accumulated in the cell nucleus, and hardly any of the fluorescence of DOX merged with lysotracker (green), which was in accordance with other reports [49]. The fluorescence intensity line of ROI across the 4T1 cells showed a complete mismatch (**Figure S5**), and the corresponding PC coefficient was determined to be 0.29. Meanwhile, in the case of

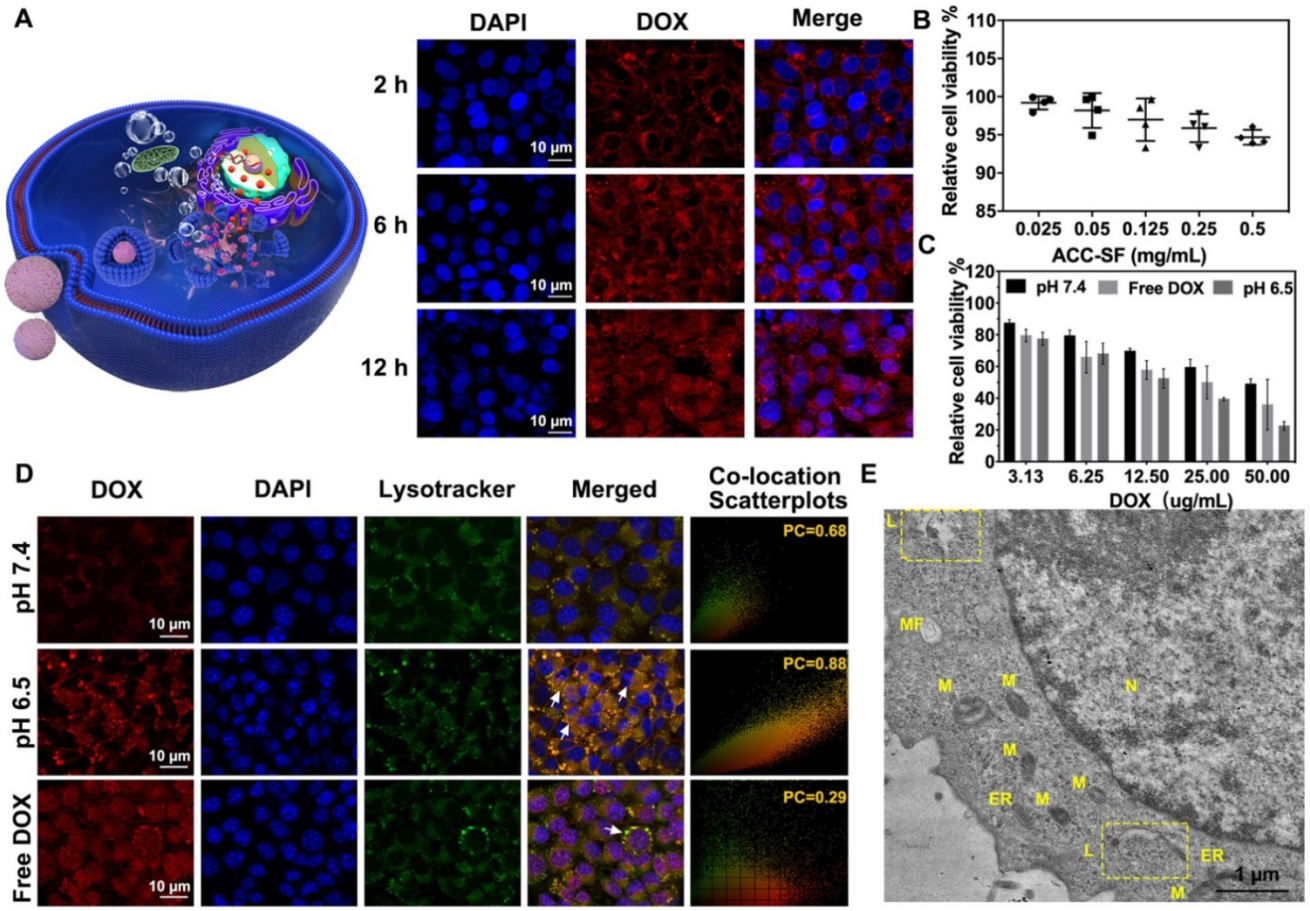

Figure 5. Intracellular DOX release from ACC-DOX-SF NPs. (A) Time-dependent (2 h, 6 h, and 12 h) intracellular uptake of ACC-DOX-SF NPs at pH 6.5 as observed by CLSM. (B) Viability assay of ACC-SF NPs incubated with HUVECs for 20 h at various concentrations. (C) Cytotoxicity assay of free DOX, ACC-DOX-SF NPs at pH 7.4, and ACC-DOX-SF NPs at pH 6.5 incubated with 4T1 cells for 24 h at different concentrations. The results are expressed as the mean ± SD, *P < 0.05, **P < 0.01, or ***P < 0.001. (D) Free DOX and ACC-DOX-SF NPs colocalized with lysosome tracker at different pH values (pH 7.4 and pH 6.5) as observed by CLSM after 3 h. For each panel, lysotracker stained the endolysosome (green); DAPI stained cell the nucleus (blue); DOX indicates NPs or drugs; and white arrows indicate NPs/ DOX located with/outside the endolysosomes, suggesting that ACC could also decompose in the cytoplasm. (E) TEM of 4T1 cells incubated with ACC-DOX-SF NPs for 4 h. The ROI (yellow square in the image) demonstrates the explosion of lysosome-targeted NPs. N, nucleus; M, mitochondria; ER, endoplasmic reticulum; L, lysosomes; MF, myelin figure.

ACC-DOX-SF NPs at pH 7.4, a small amount of immobilized DOX was retained in the cytoplasm and overlapped with lysotracker (yellow area). However, after pretreatment, the size of ACC-DOX-SF NPs decreased, which was beneficial for cellular uptake. Thus, most NPs were concentrated in the cytoplasm and merged well with lysotracker, quickly decomposing into Ca^{2+} and CO_2, and the higher internal pressure led to the destruction of lysosomes, after which the released DOX aggregated in the cell nucleus. Moreover, the fluorescence intensity line profiles of ROI of ACC-DOX-SF NPs at pH 6.5 showed almost a complete match, as supported by a high PC coefficient (PC = 0.88). To visualize the process of cellular uptake and lysosome targeting and destruction, TEM images of cells incubated with NPs for 2 h, 4 h, 6 h, 12 h were recorded, respectively. As shown in **Figure 5E** and **Figure S6**, lysosomes were characterized by an amorphous electron-dense content [50]. Some of them displayed a major morphological change, becoming swollen like a balloon, with increasingly more NPs retained inside and partly disrupted. Thus, these results firmly confirmed the good lysosome-targeting and destruction capability of ACC-DOX-SF NPs, which further promoted drug accumulation in the nucleus, causing an immediate toxicity effect in the cells.

PAI -guided drug release of ACC-DOX-SF NPs *in vivo*

PAI has been recognized as a promising technology to trace drug release behavior in tumor sites. Because CO_2 absorbs light energy at a distinct wavelength, thus locally increasing temperature, pressure fluctuations generated by the thermal expansion of this gas can be detected as acoustic waves visualized by an acoustic detector and displayed as a PA signal [51, 52]. In this study, the PA signal of ACC-DOX-SF NPs was measured by a VisualSonics Vevo LAZR at predetermined times. The optimal PA signal of ACC-DOX-SF NPs was at an excitation wavelength of ~700 nm. After the measurement device was infused with pure CO_2, a strong PA signal could be recorded (**Figure S7A**). The intensity of the PA signal of the NPs in PBS solution at pH 5.5 and 6.5 gradually increased and then slowly decreased, whereas a negligible PA signal was observed at pH 7.4 (**Figure S7B, C**) due to the very small amount of generated CO_2, which was consistent with previous similar reports [53]. Therefore, based on the PA properties of CO_2 *in vitro*, *in vivo* PAI was conducted using a Vevo LAZR system and a 700 nm laser. The PA signal of the group treated with ACC-DOX-SF NPs increased at 1 h post injection (**Figure S7D, E**). Additionally, the increased quantity of ACC-DOX-SF NPs accumulating in the tumor site decreased with time, leading to a corresponding decrease in the quantity of small bubbles converging into microbubbles, while the amount of DOX in the tumor site still increased. Notably, small CO_2 bubbles (< micrometer) had a poor echogenic sensitivity owing to the resolution of the PAI instruments (typically 50 to 100 μm) [54]. Therefore, the PAI time of the tumor was relatively short (approximately 4 h). In contrast, the group treated with saline showed nearly no PA signal for the entire time. Nevertheless, these results demonstrated that the ACC-DOX-SF NPs possessed imaging-guided tumor-specific, tumor-triggered drug release characteristics.

In vivo chemotherapeutic efficacy of ACC-DOX-SF NPs

The highly efficient lysosome targeting and prolonged circulation time *in vitro* potentially guaranteed the potential of ACC-DOX-SF NPs for cancer chemotherapy. To verify our hypothesis, a 4T1 tumor-bearing mouse model was established for *in vivo* chemotherapeutic assessment. When the tumor volume grew to 60-80 mm^3, the mice were intravenously administered with 200 μL ACC-DOX-SF NPs or free DOX (equivalent to 5 mg DOX/kg per mouse) every 5 days, and mice in the control group were treated with saline (**Figure 6A**). After 20 days of the different treatments, the mice treated with ACC-DOX-SF NPs exhibited a prominent antitumor effect, with a 2.5-fold increase in the original tumor volume compared with a 3.9-fold increase for the free DOX group, a 3.5-fold increase for the ACC-DOX NPs group and a 6.3-fold increase for the saline group (**Figure 6D**), which was consistent with the histologic indication that treatment with ACC-DOX-SF NPs resulted in large-scale apoptosis in cancer cells (**Figure 6B**). No apparent toxic effects or tumor metastasis were found in any organs (**Figure S8**), indicating the high histocompatibility of ACC-DOX-SF NPs. During the periods of treatment, the body weights of mice treated with ACC-DOX-SF NPs showed a slight increase compared with those of the saline group, while obvious weight loss was observed in the DOX-treated group (**Figure 6C**), which manifested the severe side effects on the whole body induced by free DOX.

PCNA, TUNEL and a CD31 immunohistochemical assay further confirmed the chemotherapeutic effect. Representative apoptosis-positive cells were recorded as having a dark brown nucleus in the TUNEL assay, while proliferation-positive cells were stained brown. As illustrated in **Figure 7** and **Figure S9-10**, the mice treated with ACC-DOX-SF NPs showed the highest level of cell apoptosis in the

TUNEL assay but the lowest proliferative activity in the PCNA assay compared with the groups receiving free DOX and saline. To investigate the relationship between tumor vessels and distribution of the NPs, we stained the blood vessels of tumor sections with CD31-FITC. Obviously, most ACC-DOX-SF NPs were scavenged by tumor tissue outside of the tumor vasculature, while some free DOX was accumulated mainly around the vasculature. Taken together, these results indicate that ACC-DOX-SF NPs was capable of efficiently and effectively delivering the drug from the exterior blood circulation to the interior of the tumor tissue.

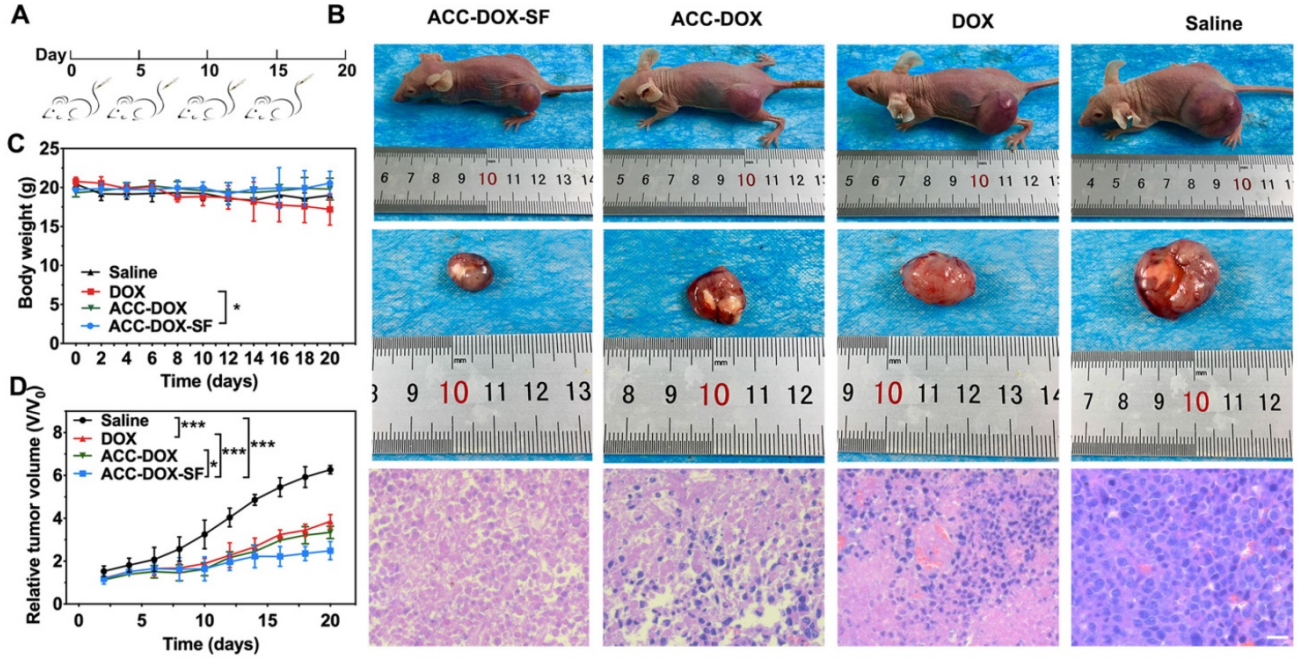

Figure 6. Evaluation of antitumor efficacy *in vivo*. (A) Schematic illustration of the treatment regimen. All groups were intravenously administered with treatments on day 0, day 5, day 10 and day 15. (B) Representative pictures of 4T1 tumor-bearing mice and H&E staining of tumor sections form mice after intravenous administration of saline, free DOX, ACC-DOX NPs and ACC-DOX-SF NPs. (C, D) Body weight changes in 4T1 tumor-bearing nude mice and tumor growth curves after intravenous administration of different treatments.

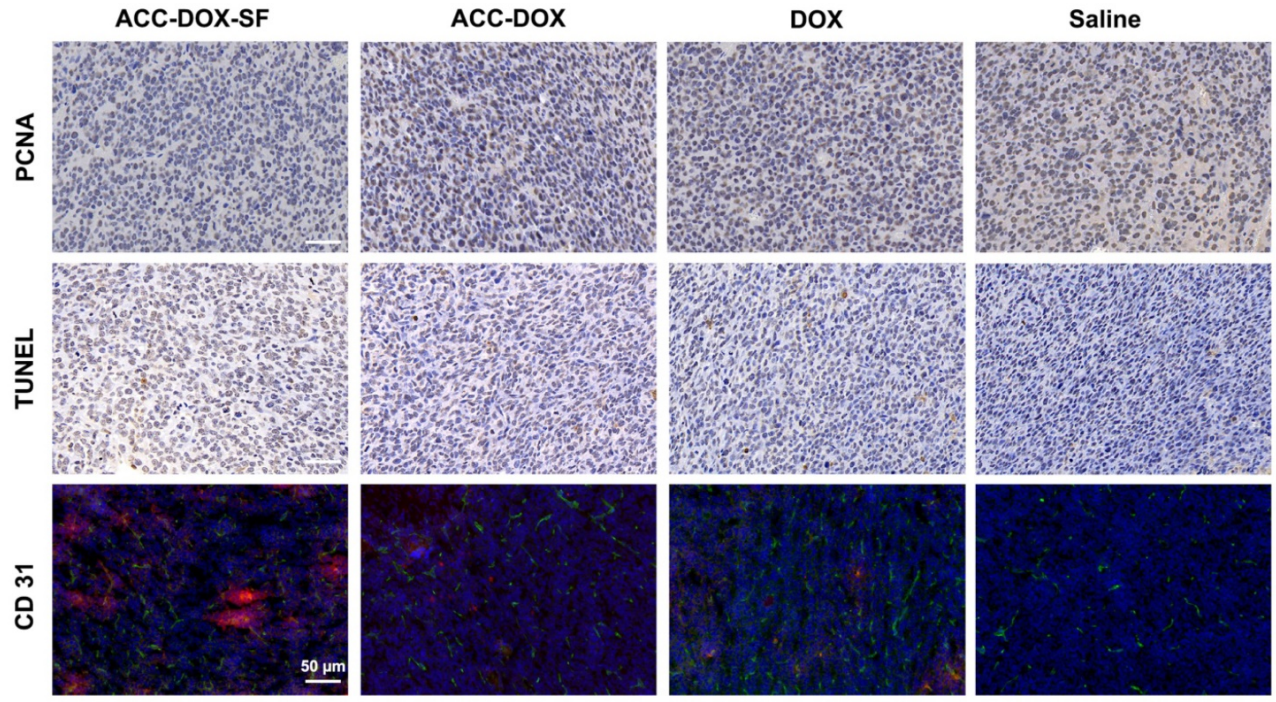

Figure 7. Immunochemical staining of PCNA and TUNEL and CD31-FITC staining of tumor sections from 4T1 tumor-bearing mice after different treatments. For CD31 images of tumor section, the nuclei were stained by DAPI (blue), CD31 was labeled with FITC (green) and DOX presented as red. The scale bars are 50 μm.

Additionally, it was highly significant for ACC-DOX-SF NPs to have highly compatibility to guarantee their further clinical translation. Therefore, the *in vivo* biosafety assay of ACC-DOX-SF NPs were evaluated in healthy Balb/c mice. At 1 h, 3 h, 6 h, 12 h, 24 h, 48 h, 72 h after intravenous administration of the ACC-DOX-SF NPs (equivalent to 5 mg DOX/kg per mouse), hematological analysis and serum biochemistry tests were performed, respectively (**Table S7**). Compared to reference range, all blood routine, liver and kidney function indicators in both blank control groups and treated groups remained at normal levels. Moreover, the immuntoxicity evaluation was conducted. According to the American National Toxicology Program for immuntoxicity of mice [55], we explored the side-effects of ACC-DOX-SF NPs and ACC-SF NPs from cellular immunity and humoral immunity in Balb/c mice. As shown in **Figure S11-12**, the percentage of $CD8^+$ T cells in group of ACC-DOX-SF NPs and DOX were lower than the control group after 7 days of injection. Besides, the percentage of $CD4^+$, $CD8^+$ T cells in group of ACC-DOX-SF NPs, ACC-SF NPs and DOX showed no significant difference compared with control group during 14 days treatment. Moreover, compared with control groups (**Figure S13-15)**, the IgM, IgG and IgA levels of mice treated with ACC-DOX-SF NPs or ACC-SF NPs showed no significant difference during the 14-day observation period. These results strongly demonstrated that the ACC-DOX-SF NPs owned the desirable high biosafety, which provide a great possibility for further clinical translation.

Conclusions

In summary, we successfully constructed TME-responsive biocompatible NPs by coating DOX-preloaded ACC-DOX clusters with SF. This natural SF served as both a modifier and gatekeeper to inhibit premature drug leakage. After being transported from the blood vessels to lysosomes in tumor cells, ACC-DOX-SF NPs were exposed to various acidic environments. These experiments showed different TME responsivities upon encountering acidic- environments, and these nanoparticles gradually degraded into smaller particles and eventually decomposed into Ca^{2+} and CO_2, which was beneficial to cellular uptake and PA monitoring. The DOX released from cracked lysosomes accumulated in the nucleus to efficiently kill tumor cells. Moreover, the bioinspired eco-friendly drug carrier ACC-SF NPs showed excellent biocompatibility *in vivo* and *in vitro* and drastically decreased the side effects of free drugs, which was promising for clinical translation.

Abbreviations

ACC: amorphous calcium carbonate; BCA: bicinchoninic acid; $CaCl_2 \cdot 2H_2O$: calcium chloride dihydrate; CCK-8: Cell Counting Kit-8; CLSM: confocal laser scanning microscope; DAPI: 2-(4-Amidinophenyl)-6-indolecarbamidinedihydrochloride; DLS: dynamic light scattering; DOX: Doxorubicin hydrochloride; FBS: fetal bovine serum; FCM: flow cytometry; H&E: hematoxylin and eosin; MDR: multidrug resistance; Na_2CO_3: sodium carbonate; NH_4HCO_3: Ammonia bicarbonate; PBS: phosphate buffered saline; PA: photoacoustic; PAI: photoacoustic imaging; PC: Pearson's correlation; PCNA: Proliferating cell nuclear antigen; ROI: region of interest; SF: silk fibroin; TEM: transmission electron microscope; TME: tumor microenvironment; TUNEL: TdT-mediated dUTP Nick-End Labeling; IgG: immunoglobulin G; IgA: immunoglobulin A; IgM: immunoglobulin M.

Supplementary Material

Supplementary figures and tables.
http://www.thno.org/v09p0961s1.pdf

Acknowledgements

We greatly acknowledge the financial support from the National Natural Science Foundation of China (81630047, 81471713, 81401503, 31630026), China Postdoctoral Science Foundation funded projects (2015T80963, 2016M590869), the National Key Research and Development Program of China (Grant No. 2016YFA0203700) and a Chongqing Postdoctoral Science Foundation funded project (Xm2015089). All animal experiments were in accordance with the Guide for Care and Use of Laboratory Animals and approved by the Animal Ethics Committee of Chongqing Medical University.

Competing Interests

The authors have declared that no competing interest exists.

References

1. Wilhelm S, Tavares AJ, Dai Q, et al. Analysis of nanoparticle delivery to tumours. Nat Rev Mater. 2016; 1: 16014.
2. O'Brien ME, Wigler N, Inbar M, et al. Reduced cardiotoxicity and comparable efficacy in a phase III trial of pegylated liposomal doxorubicin HCl (CAELYX/Doxil) versus conventional doxorubicin for first-line treatment of metastatic breast cancer. Ann Oncol. 2004; 15 (3): 440-9.
3. Judson I, Radford JA, Harris M, et al. Randomised phase II trial of pegylated liposomal doxorubicin (DOXIL/CAELYX) versus doxorubicin in the treatment of advanced or metastatic soft tissue sarcoma: a study by the EORTC soft tissue and bone sarcoma group. Eur J Cancer. 2001; 37 (7): 870-7.
4. Halford S, Yip D, Karapetis CS, et al. A phase II study evaluating the tolerability and efficacy of CAELYX (liposomal doxorubicin, Doxil) in the treatment of unresectable pancreatic carcinoma. Ann Oncol. 2001; 12 (10): 1399-402.
5. You HB, Park K. Targeted drug delivery to tumors: myths, reality and possibility. J Control Release. 2011; 153: 198-205.

6. Jmm L, Towers CG, Thorburn A. Targeting autophagy in cancer. Nat Rev Cancer. 2017;17: 528–42.
7. Settembre C, Fraldi A, Medina DL, et al. Signals for the lysosome: a control center for cellular clearance and energy metabolism. Nat Rev Mol Cell Biol. 2013; 14: 283-96.
8. Gao W, Cao WH, Zhang HB, et al. Targeting lysosomal membrane permeabilization to induce and image apoptosis in cancer cells by multifunctional Au-ZnO hybrid nanoparticles. Chem Commun (Camb). 2014; 50: 8117-20.
9. Ge W, Li D, Gao Y, Cao X. The Roles of lysosomes in inflammation and autoimmune diseases. Int Rev Immunol. 2015; 34: 415-31.
10. Pan W, Wang HH, Yang LM, et al. Ratiometric fluorescence nanoprobes for subcellular pH imaging with a single-wavelength excitation in living cells. Anal Chem. 2016; 88: 6743-48.
11. Zhou J, Shi W, Li LH, et al. A lysosome-targeting fluorescence off-on probe for imaging of nitroreductase and hypoxia in live cells. Chem Asian J. 2016; 11: 2719.
12. Wang L, Xiao Y, Tian WM, Deng LZ. Activatable rotor for quantifying lysosomal viscosity in living cells. J Am Chem Soc. 2013; 135: 2903-6.
13. Wan Q, Chen S, Shi W, et al. Lysosomal pH rise during heat shock monitored by a lysosome-targeting near-infrared ratiometric fluorescent probe. Angew Chem Int Ed Engl. 2014; 53 (41): 10916-20.
14. Jing XT, Yu FB, Chen LX. Visualization of nitroxyl (HNO) in vivo via a lysosome-targetable near-infrared fluorescent probe. Chem Commun (Camb). 2014; 50 (91): 14253-6.
15. Yang Y, Jing L, Li X, et al. Hyaluronic acid conjugated magnetic prussian blue@quantum dot nanoparticles for cancer theranostics. Theranostics. 2017; 7 (2): 466-81.
16. Cheng K, Sano M, Jenkins C, et al. Synergistically enhancing therapeutic effect of radiation therapy with radiation activatable and reactive oxygen species-releasing nanostructures. ACS Nano. 2018; 12 (5): 4946-58.
17. Zhou Q, Hou Y, Zhang L, et al. Dual-pH sensitive charge-reversal nanocomplex for tumor-targeted drug delivery with enhanced anticancer activity. Theranostics. 2017; 7 (7): 1806-19.
18. Yu Z; Sun Q; Pan W, et al. A near-infrared triggered nanophotosensitizer inducing domino effect on mitochondrial reactive oxygen species burst for cancer therapy. ACS Nano. 2015; 9 (11): 11064-74.
19. Montalbán MG, Coburn JM, Lozano-Pérez AA, et al. Production of curcumin-loaded silk fibroin nanoparticles for cancer therapy. Nanomaterials. 2018; 8:2.
20. Lozano-Pérez AA, Rivero HC, Pérez Hernández MDC, et al. Silk fibroin nanoparticles: Efficient vehicles for the natural antioxidant quercetin. Int J Pharm. 2017; 518(1–2): 11-19.
21. Tian Y, Jiang X, Chen X, et al. Doxorubicin-loaded magnetic silk fibroin nanoparticles for targeted therapy of multidrug-resistant cancer. Adv Mater. 2014; 26: 7393–7398.
22. Seib FP, Jones GT, Rnjak-Kovacina J, et al. pH-dependent anticancer drug release from silk nanoparticles. Adv Healthc Mater. 2013; 2: 1606-11.
23. Seib FP, Maitz MF, Hu X, et al. Impact of processing parameters on the haemocompatibility of Bombyx mori silk films. Biomaterials. 2012; 33: 1017-23.
24. Wenk E, Merkle HP, Meinel L. Silk fibroin as a vehicle for drug delivery applications. J Control Release. 2011; 150: 128–41.
25. Von KC, Fidler I, Deimling AV, et al. Growth and metastasis of tumor cells isolated from a human renal cell carcinoma implanted into different organs of nude mice. Cancer Res. 1986; 46(8):4109.
26. Euhus DM, Hudd C, LaRegina MC, et al. Tumor measurement in the nude mouse. J Surg Oncol. 1986; 31: 229-34.
27. Tomayko MM, Reynolds CP. Determination of subcutaneous tumor size in athymic (nude) mice. Cancer Chemother Pharmacol. 1989; 24(3):148-154.
28. Zhao Y, Lin LN, Lu Y, et al. Templating synthesis of preloaded Doxorubicin in hollow mesoporous silica nanospheres for biomedical applications. Adv Mater. 2010; 22 (46): 5255-9.
29. Kato T, Sugawara A, Hosoda N. Calcium Carbonate–Organic Hybrid Materials. Adv Mater. 2010; 14: 869-77.
30. Chen Y, Wan Y, Wang Y, et al. Anticancer efficacy enhancement and attenuation of side effects of doxorubicin with titanium dioxide nanoparticles. Int J Nanomedicine. 2011; 6: 2321-6.
31. Cheung BC, Sun TH, Leenhouts JM, Cullis PR. Loading of doxorubicin into liposomes by forming Mn^{2+}-drug complexes. Biochim BIophys Acta.1998; 1414(1-2): 205-16.
32. Deng Y, Zhang H. The synergistic effect and mechanism of doxorubicin-ZnO nanocomplexes as a multimodal agent integrating diverse anticancer therapeutics. Int J Nanomedicine. 2013; 8: 1835-41.
33. Chen Y, Wan Y, Wang Y, et al. Anticancer efficacy enhancement and attenuation of side effects of doxorubicin with titanium dioxide nanoparticles. Int J Nanomedicine. 2011; 6: 2321-6.
34. Faatz M, Gröhn F, Wegner G. Amorphous calcium carbonate:synthesis and potential intermediate in biomineralization. Adv Mater. 2010; 16: 996-1000.
35. Chen SF. Ethanol assisted synthesis of pure and stable amorphous calcium carbonate nanoparticles. Chem Commun (Camb). 2013: 49; 9564-6.
36. Addadi L, Raz S, Weiner S. Taking advantage of disorder: amorphous calcium carbonate and its roles in biomineralization. Adv Mater. 2003: 15:959-70.
37. Rodriguez-Blanco JD, Shaw S, Benning LG. The kinetics and mechanisms of amorphous calcium carbonate (ACC) crystallization to calcite, via vaterite. Nanoscale. 2011; 3: 265-71.
38. Rodriguez-Blanco JD, Shaw S, Benning LG, How to make 'stable' ACC: protocoland preliminary structural characterization. Mineral Mag. 2008; 72: 283–6.
39. Wang Y, Zhou K, Huang G, et al. A nanoparticle-based strategy for the imaging of a broad range of tumours by nonlinear amplification of microenvironment signals. Nat Mater. 2014; 13: 204-12.
40. Chauhan VP, Stylianopoulos T, Martin JD, et al. Normalization of tumour blood vessels improves the delivery of nanomedicines in a size-dependent manner. Nat Nanotechnol. 2012; 7: 383-8
41. Wang C, Chen Shaoqing, et al. Lipase-triggered water-responsive "pandora's box" for cancer therapy: toward induced neighboring effect and enhanced drug penetration. Adv Mater. 2018; 30(14): e1706407.
42. Salzano G, Costa DF, Sarisozen C, et al. Mixed nanosized polymeric micelles as promoter of doxorubicin and miRNA-34a co-delivery triggered by dual stimuli in tumor tissue. Small. 2016; 12: 4837-48.
43. Karemore MN, Avari JG. Zeta potential as a novel diagnostic tool for preeclampsia. Pregnancy Hypertens. 2018; 13: 187-197.
44. Morrison ID, Ross S. Colloidal dispersions: suspensions, emulsions and foams. New York, USA: John Wiley & Sons Publisher; 2002.
45. Van AJ, Van TO, Beijnen JH. Determination of doxorubicin and metabolites in murine srecimens by high-performance liquid chromatography. J Chromatogr B Biomed Sci Appl. 1998; 712 (1-2): 129-43.
46. Camaggi CM, Comparsi R, Strocchi E, et al. HPLC analysis of doxorubicin, epirubicin and fluorescent metabolites in biological fluids. Cancer Chemother Pharmacol. 1988; 21(3): 216-20.
47. Choi HS, Liu W, Misra P, et al. Renal clearance of quantum dots. Nat Biotechnol. 2007; 25 (10): 164-8.
48. Gustafson DL, Rastatter JC, Colombo T, Long ME. Doxorubicin pharmacokinetics: Macromolecule binding, metabolism, and excretion in the context of a physiologic model. J Pham Sci. 2002; 91(6): 1488-501.
49. Zhao Y, Luo Z, Li M, et al. A preloaded amorphous calcium carbonate/doxorubicin@silica nanoreactor for pH-responsive delivery of an anticancer drug. Angew Chem Int Engl. 2015; 54 (3): 919 –22.
50. Mauthe M, Orhon I, Rocchi C, et al. Chloroquine inhibits autophagic flux by decreasing autophagosome-lysosome fusion. Autophagy. 2018; 14: 1435-55.
51. Navas MJ, Jiménez AM, Asuero AG. Human biomarkers in breath by photoacoustic spectroscopy. Clin Chim Acta. 2012; 413: 1171-8.
52. Ivascu IR, Matei CE, Patachia M, et al. CO_2 laser photoacoustic measurements of ethanol absorption coefficients within infrared region of 9.2-10.8 mum. Spectrochim Acta A Mol Biomol Spectrosc. 2016; 163: 115-9.
53. Xia J, Feng G, Xia X, et al. NH_4HCO_3 gas-generating liposomal nanoparticle for photoacoustic imaging in breast cancer. Int J Nanomedicine. 2017; 12: 1803-13.
54. Lindner JR. Microbubbles in medical imaging: current applications and future directions. Nat Rev Drug Discov. 2004; 3: 527-32.
55. National toxicology program. NTP toxicology and carcinogenesis studies of malonaldehyde, sodium salt (3-hydroxy-2-propenal, sodium salt) (CAS No. 24382-04-5) in F344/N rats and B6C3F1 mice (gavage studies). Nati Toxicol Program Tech Rep Ser. 1988; 331:1-182.